Acoustic radiation of a fluid-saturated microperforated plate

Lucie Gallerand, Mathias Legrand, Raymond Panneton, Philippe Leclaire, Thomas Dupont

Acoustic radiation of a fluid-saturated microperforated plate

Lucie Gallerand[a], Mathias Legrand[b,c], Raymond Panneton[d], Philippe Leclaire[e], Thomas Dupont[a]

[a] *Department of Mechanical Engineering, École de technologie supérieure, Montréal, Canada*
[b] *Department of Mechanical Engineering, McGill University, Montréal, Canada*
[c] *Nantes Université, Ecole Centrale Nantes, CNRS, GeM, UMR 6183, F-44000 Nantes, France*
[d] *CRASH-UdeS, Department of Mechanical Engineering, Université de Sherbrooke, Sherbrooke, Canada*
[e] *DRIVE, Université Bourgogne Europe, ISAT, Nevers, France*

Abstract

Microperforated plates (MPPs) are widely used for their acoustic absorption capabilities. Recent studies have further shown that they can effectively mitigate low-frequency structural vibrations through viscous added damping: the oscillatory air motion induced by plate vibration generates viscothermal losses within the perforation boundary layers, thereby dissipating mechanical energy. However, the influence of this added damping on the acoustic radiation of MPPs has not yet been thoroughly investigated. This article addresses this gap by analyzing the vibroacoustic behavior of MPPs immersed in a light fluid, with particular emphasis on the role of viscous damping in shaping the radiated sound field. To this end, an analytical model is developed based on an ad hoc homogenization procedure derived from the Biot's theory. This approach provides a unified description of both the solid displacement field and the relative fluid–solid motion within the perforations. From the resulting displacement fields, the vibroacoustic indicators are computed, including mean square velocity, radiated acoustic power, and radiation efficiency, for varying perforation rates and fluid properties. The results demonstrate that viscothermal losses in the perforations significantly reduce vibration amplitude and radiation efficiency, particularly in the vicinity of the first structural resonance. The results further reveal an interesting phenomenon: the oscillating fluid columns within the perforations act as air pistons that can locally increase radiated power compared to a solid plate. Nevertheless, the overall radiation efficiency systematically decreases due to the combined effects of reduced radiating surface area, additional damping, and permeability to fluid flow. The analytical predictions are validated against finite element simulations using a fully coupled ThermoViscous Acoustic model, with good agreement confirming the accuracy of the proposed approach and highlighting the key physical mechanisms governing sound radiation from microperforated structures. Finally, the near-to-far field transition is investigated both analytically and numerically, revealing that the transition distance is governed by the plate dimensions and the perforation parameters, namely hole diameter, spacing, and frequency.

Keywords: Microperforated plate — Sound radiation — Fluid-solid interaction — Viscous dissipation

Contents

Email addresses: lucie.gallerand@etsmtl.ca (Lucie Gallerand), mathias.legrand@mcgill.ca (Mathias Legrand), raymond.panneton@USherbrooke.ca (Raymond Panneton), philippe.leclaire@u-bourgogne.fr (Philippe Leclaire), thomas.dupont@etsmtl.ca (Thomas Dupont)

Nomenclature

Geometric constants

d	diameter of perforation (m)
h	plate/MPP thickness (m)
L_x	plate/MPP length in x direction (m)
L_y	plate/MPP length in y direction (m)
$\mathbf{x} = (x, y)$	space coordinates

Macroscopic parameters

α_∞	tortuosity
δ_v	thickness of viscous boundary layer (m)
$\phi(\mathbf{x})$	spatial perforation ratio
ϕ_0	perforation ratio
σ	fluid flow resistivity ($\mathrm{N\,s\,m^{-4}}$)
f_c	characteristic frequency (Hz)

Mechanical parameters

α	Biot's elastic coupling coefficient
η_s	isotropic structural loss factor
μ_f	fluid dynamic viscoelasticity ($\mathrm{kg\,m^{-1}\,s^{-1}}$)
ν_0	Poisson's coefficient
ρ	mixture density ($\mathrm{kg\,m^{-3}}$)
ρ_f	fluid density ($\mathrm{kg\,m^{-3}}$)
ρ_s	structure density ($\mathrm{kg\,m^{-3}}$)
D	bending stiffness (N m)
$D^*(\phi_0)$	complex equivalent bending stiffness (N m)
E	Young's modulus (Pa)
K_f	fluid bulk modulus (Pa)
M_f	Biot's elastic coefficient ($\mathrm{N\,m^{-2}}$)

Other parameters

$G(\mathbf{x}, \mathbf{x}_1)$	Green function used for sound radiation
$f_\mathrm{ext}(\mathbf{x}, t)$	external force (N)
P_0	magnitude of the external pressure (Pa)
ω	angular frequency ($\mathrm{rad\,s^{-1}}$)
N	number of degrees-of-freedom
$\Psi_{mn}(\mathbf{x})$	modal shape of mode mn
$w_\mathrm{s}(\mathbf{x}, t)$	solid displacement (m)
$w(\mathbf{x}, t)$	fluid-solid relative displacement (m)
$w_\mathrm{tot}(\mathbf{x}, t)$	total displacement: $w(\mathbf{x}, t) + w_\mathrm{s}(\mathbf{x}, t)$

Vibroacoustic indicators

s	radiation efficiency
V^2	mean square velocity ($\mathrm{m^2\,s^{-2}}$)
W	radiated sound power (Pa)
Z_{ik}	ik-th entry of the radiation impedance matrix

1. Introduction

Structural vibrations and more specifically low frequency (LF) structural vibrations can be a significant source of noise. Conventional noise control techniques often aim at reducing vibration amplitude through damping treatments, vibration isolation, or structural modifications. However, these approaches typically add mass to the structure, which conflicts with current trends toward lightweight design for reduced energy consumption, costs, and environmental impact. An alternative approach consists in directly reducing the sound radiation of plate-like structures by manufacturing them from perforated materials [1], thereby achieving noise reduction while simultaneously reducing structural mass. Recent work by the authors showed that it is also possible to directly mitigate LF vibrations through microperforated plate (MPP) systems [2, 3]. Beyond their role as radiating structures, MPP are also widely employed as lightweight solutions for sound absorption, offering an effective alternative to porous media and conventional resonant systems [4]. Their simple design and adaptability to a broad range of base materials [5] confer them enhanced durability, environmental compatibility, and reduced risks of material degradation, while preserving their lightweight characteristics. These properties have enabled their use across a wide variety of applications, from acoustic enclosures and duct linings in flow environments [6] to more demanding contexts such as nuclear engines and reactors [7]. When coupled with a backing air cavity, MPP form effective acoustic absorbers that exploit both the resistive and reactive viscothermal effects occurring within the perforations [8, 9, 10]. In addition to these acoustic mechanisms, an extra structural damping has been shown to arise arround a characteristic frequency, driven by dissipative effects within the thermoviscous boundary layers at the fluid–solid interface of the perforations [2, 3]. Research has also focused on the relationship between MPP vibrations and their acoustic signature. Under acoustic excitation, viscothermal boundary layers develop inside the microperforations and couple the fluid motion to the surrounding structure, such that even low-amplitude excitations can drive significant panel vibrations [11]. Capturing this fluid–structure interaction accurately is therefore essential, yet early studies relied on electroacoustic analogies that combined acoustic and structural effects as impedances in parallel [12, 10], effectively neglecting such interactions. Such fluid-structure interactions were first investigated by Takahashi and Tanaka [13] who introduced the concept of relative velocity between fluid and solid based on Biot's theory [14, 15] coupled with Maa's impedance model [16]. They showed that plate elasticity, perforation geometry, and viscothermal boundary layers govern the acoustic absorption [17, 18]. Building on these ideas, Putra and Thompson [1, 19] demonstrated that perforating a vibrating plate reduces its sound

radiation efficiency, with the reduction governed by both the perforation ratio and the hole size. Their analytical models accurately predicted the radiation efficiency across a wide range of vibrational modes and were validated experimentally. More recent studies extend these insights. Zhu *et al.* [20] showed that the arrangement of holes and the implementation of additional absorbing layers can significantly modify the radiated power, offering new avenues for controlling structural acoustics. Subsequent works investigated cavity-coupled systems [21]. An absorption peak or dip can occur depending on whether the structural resonance frequency lies above or below the acoustic resonance frequency of the backed MPP system, a phenomenon explained by the normalized resistance and the phase relationship between the vibrating panel and the acoustic wave. Lee *et al.* showed that MPP vibrations broaden these absorption features when combined with viscothermal dissipation [22, 23], and Toyoda *et al.* further identified two distinct absorption mechanisms related to structural modes and mass–spring resonances [24]. Modal approaches were later developed by Bravo *et al.* [25, 11, 26, 27], confirming the importance of relative velocity and the influence of boundary conditions. To more accurately capture the effect of membrane flexibility on perforation impedance, Li *et al.* [28] proposed a model based on a no-slip boundary condition at the perforation wall, whereby the acoustic impedance of each hole varies with its location on the vibrating membrane, while Tournadre *et al.* [29] used finite element methods to highlight the role of boundary conditions in coupled vibroacoustic systems. Independently, it has also been shown that a MPP can be modeled as an equivalent porous plate [9]. Building on this observation, Gallerand *et al.* [2] developed an analytical model for the vibration analysis of MPP from a porous plate model [30]. The model showed that dissipation mechanisms depend on the perforation diameter, with added damping being increasingly effective as frequency decreases [2]. In practice, the characteristic frequency is tuned to coincide with the natural frequency of the mode to be damped. Damping effectiveness can be further enhanced by concentrating perforations at modal antinodes and ensuring a high local porosity in those regions [3]. More recently, it was shown with a nonlinear model that beyond a certain excitation level, the damping becomes amplitude-dependent [31]. During plate oscillation, boundary layers develop within the microperforations, driving fluid motion that couples with the solid's vibrations. While these damping mechanisms are well-understood, their specific impact on the structure's acoustic radiation remains unexplored. A related problem, that of vibrations in porous plates loaded with fluid [32], has been addressed using classical vibroacoustic approaches for radiating plates [33, 34], which provide an appropriate methodological basis for extension to MPP. In the present work, an analytical model is developed by adapting the vibroacoustic theory of thin plates [33, 34], previously used for porous plates [32], to microperforated plates. Based on [2], Section 2.1 recalls the governing equation describing the vibroacoustic response of a MPP saturated with and loaded by a lightweight fluid. Then, Section 3 provides a parametric analysis highlighting the respective contributions of the fluid and solid phases, while Section 4 reports a numerical validation carried out using COMSOL Multiphysics. Finally, Section 5 proposes a discussion on near-field/far-field transition distances, thereby establishing the limits of the homogenized model.

2. Theoretical background

2.1. Governing equations for the fluid-saturated microperforated plate

This section restates briefly the equations developed and validated in ref. [2], thereby ensuring that the paper is sufficiently self-contained; some elements are deliberately repeated for the sake of clarity. The investigated structure is a baffled rectangular microperforated plate of dimension $L_x \times L_y \times h$ oriented in the xy plane, as sketched in Figure 1. The plate can be forced mechanically by a driving external point force $f_{\text{ext}}(\mathbf{x}, t) = F_{\text{ext}}(t)\delta(\mathbf{x} - \mathbf{x}_0)$ where F_{ext} is the applied force, δ, the two-dimensional Dirac distribution, and $\mathbf{x}_0$, the point force. It can also be forced acoustically by a pressure difference between the two planes $z = -h/2$ and $z = +h/2$, or acoustically and mechanically through a combination of the two external excitations. The point $\mathbf{x} = (x, y)$ corresponds to the space coordinates. The baffle is fixed at $z = 0$ and separates the plate from two infinite fluid domains ($z > \pm h/2$). Using an alternative form of Biot's theory, the model developed in the framework of porous plates in [30] is adapted to an MPP. An *ad hoc* homogenization procedure is performed [14, 15], leading to two coupled partial differential equations (PDEs) that govern the dynamics of an effective structural plate and a virtual fluid plate

$$h(\rho\ddot{w}_{\text{s}}(\mathbf{x}, t) + \rho_{\text{f}}\ddot{w}(\mathbf{x}, t)) + D^*\nabla^4 w_{\text{s}}(\mathbf{x}, t) = f_{\text{ext}}(\mathbf{x}, t) + 2p(\mathbf{x}, t), \tag{1a}$$

$$\rho_{\text{f}} h\ddot{w}_{\text{s}}(\mathbf{x}, t) + \frac{h\rho_{\text{f}}\alpha_\infty}{\phi_0}\ddot{w}(\mathbf{x}, t) + h\sigma\dot{w}(\mathbf{x}, t) + h\alpha M_{\text{f}}\nabla^2 w_{\text{s}}(\mathbf{x}, t) = \phi_0 p(\mathbf{x}, t), \tag{1b}$$

where $w_{\text{s}}(\mathbf{x}, t)$ is the solid motion displacement and $w(\mathbf{x}, t)$ corresponds to the relative fluid-solid motion displacement. The complex coefficient D^* is the effective bending stiffness of the perforated plate (its explicit expression is given in Equation (3) below).

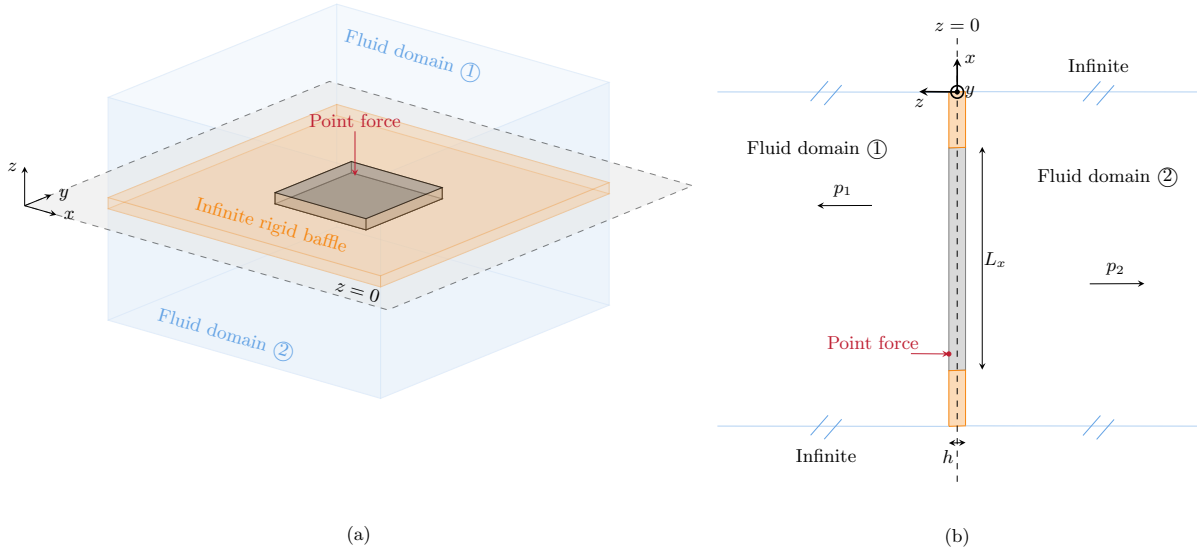

(a) (b)

Figure 1: System of coordinates and the geometry of the investigated baffled microperforated plate in (a) the 3D view and in (b) a sectional view along the xz plane.

Under acoustic excitation, the plate vibrates and radiates normal pressure waves on both sides of the plate, *i.e.* in the half-spaces $z < -h/2$ and $z > h/2$. At the plate surface $z = \pm h/2$, the total acoustic pressure acting on the structure corresponds to the so-called blocked pressure $P_b = 2P_0$ [35]. Accordingly, the external loading term in the governing equation (1a) of the equivalent solid plate is expressed as $2p(\mathbf{x}, t)$. Imposing this blocked pressure is equivalent to applying a normally incident plane wave of amplitude P_0 [35]. For an MPP, the surface occupied by the saturating fluid represents a fraction ϕ_0 of the total surface. Thus, assuming that the acoustic pressure is zero behind the plate (*i.e.* $z > h/2$), the stress applied on the equivalent fluid plate is taken as $\phi_0 p$ to account for the fact that the pressure difference p applies only to the fluid surface [30]. In this paper, the focus is on the structural response, so the acoustic pressure term $p(\mathbf{x}, t)$ is set to zero, with any acoustic forcing being representable later as an equivalent mechanical load. In Equation (1a), the fluid-solid mixture density is described by

$$\rho = (1 - \phi_0)\rho_\mathrm{s} + \phi_0 \rho_\mathrm{f}, \tag{2}$$

where ρ_s and ρ_f are respectively the solid and fluid densities, ϕ_0 being the perforation ratio. In order to consider the sensitivity of the MPP stiffness to the microperforations, an equivalent bending stiffness coefficient is defined; it reads [36]

$$D^*(\phi_0) = \frac{EC(\phi_0)h^3}{12(1-\nu^2)}(1 + j\eta_\mathrm{s}) \quad \text{with} \quad C(\phi_0) = \frac{(1-\phi_0)^2}{1 + (2 - 3\nu)\phi_0}, \tag{3}$$

where E and ν are respectively Young's modulus and Poisson's ratio of the non-perforated plate. The structural loss factor η_s is used in Equation (3) to account for structural damping. The parameters α and M_f are the elastic coefficients defined by Biot [37]. Equation (1a) represents the elastic response of the homogeneous solid plate while Equation (1b) describes the relative fluid-solid motion. Elastic interactions are quantified by the α-dependent term. Inertial interactions are described by the acceleration terms. In this model, all Johnson-Champoux-Allard (JCA) macroscopic parameters defined for a porous medium can be translated to an MPP as being functions of ϕ_0 and the perforation diameter d [2], so that static airflow resistivity and tortuosity are defined for circular straight perforations by

$$\sigma(\phi_0, d) = \frac{32\mu_\mathrm{f}}{\phi_0 d^2} \quad \text{and} \quad \alpha_\infty(\phi_0, d) = 1 + \frac{2\epsilon(\phi_0, d)}{h}, \tag{4}$$

where μ_f is the fluid dynamic viscosity and $\epsilon(\phi_0, d) = 0.24\sqrt{\pi d^2}(1 - 1.14\sqrt{\phi_0})$ [9] is an end correction factor used to consider the fluid radiation inside the perforations and the distortion of the fluid flow at the perforation orifices[1]. The viscous and thermal characteristic lengths are both equal to $\Lambda = \Lambda' = d/2$ for circular straight perforations. For an MPP, the added damping is maximal at the *characteristic*

[1] Following [9], the upper limit of ϕ is set to 16% in this paper.

frequency [2]

$$f_c(d) = \frac{32\mu_f}{2\pi\alpha_\infty \rho_f d^2}. \tag{5}$$

In the present study, the perforation diameter d is chosen such that $f_c(d)$ coincides with the first resonance frequency of the MPP, in order to assess the effect of maximum viscous damping on the acoustic radiation.

2.2. Solution procedure

Solutions in terms of $w_s(\mathbf{x}, t)$ and $w(\mathbf{x}, t)$ are developed on the basis of orthogonal or quasi-orthogonal eigenfunctions. The plate displacement and the relative fluid-solid displacement are assumed to be of the form

$$w_s(\mathbf{x}, t) = \sum_{i=1}^{N} \Psi_i(\mathbf{x}) w_i^s(t) \quad \text{and} \quad w(\mathbf{x}, t) = \sum_{i=1}^{N} \Psi_i(\mathbf{x}) w_i(t), \tag{6}$$

where $\Psi_i(\mathbf{x})$, $i = 1, \ldots, N$, are the eigenmodes of the non-perforated plate, determined from the boundary conditions. Each mode is a function expressed as a linear combination of sine and cosine terms, and the set of modes is gathered in the column vector $\mathbf{\Psi}(\mathbf{x})$[2]. The corresponding modal participations are noted $w_i^s(t)$ and $w_i(t)$ respectively for the solid and the relative fluid-solid motion and N is the number of degrees-of-freedom (dof) in the discretization. Approximations in Equation (6) are inserted in Equation (1) and a classical Galerkin-like projection is performed, to generate a system of ordinary differential equations (ODEs) for the modal amplitudes $w_i(t)$ and $w_i^s(t)$. The resulting system is written in the matrix form

$$\mathbf{A}\dot{\mathbf{z}}(t) + \mathbf{B}\mathbf{z}(t) = \mathbf{Q}(t) \quad \text{with} \quad \mathbf{Q}(t) = \begin{pmatrix} 0 \\ \mathbf{F}_{\text{ext}}(t) + \mathbf{P}_1(t) \\ \mathbf{P}_2(t) \end{pmatrix} \quad \text{and} \quad \mathbf{z}(t) = \begin{pmatrix} \mathbf{w}_s(t) \\ \dot{\mathbf{w}}_s(t) \\ \dot{\mathbf{w}}(t) \end{pmatrix}, \tag{7}$$

where

$$\mathbf{A} = \begin{bmatrix} \mathbf{I_d} & \mathbf{0} & \mathbf{0} \\ \mathbf{0} & \mathbf{M}_1 & \mathbf{M} \\ \mathbf{0} & \mathbf{M} & \mathbf{M}_2 \end{bmatrix}, \quad \mathbf{B} = \begin{bmatrix} \mathbf{0} & -\mathbf{I_d} & \mathbf{0} \\ \mathbf{K}_1 & \mathbf{0} & \mathbf{0} \\ \mathbf{K}_2 & \mathbf{0} & \mathbf{C} \end{bmatrix}. \tag{8}$$

Vectors $\mathbf{w}_s(t)$ and $\dot{\mathbf{w}}(t)$ store the modal participations for both solid and relative fluid-solid motion. Matrices in Equation (7) are defined as follows:

$$\begin{aligned} &\mathbf{M}_1 = h\rho \int_S \mathbf{\Psi}\mathbf{\Psi}^\top \, \mathrm{d}\mathbf{x}, \quad \mathbf{M}_2 = \frac{h\rho_f \alpha_\infty}{\phi_0} \int_S \mathbf{\Psi}\mathbf{\Psi}^\top \, \mathrm{d}\mathbf{x}, \quad \mathbf{M} = h\rho_f \int_S \mathbf{\Psi}\mathbf{\Psi}^\top \, \mathrm{d}\mathbf{x}, \\ &\mathbf{C} = h\sigma \int_S \mathbf{\Psi}\mathbf{\Psi}^\top \, \mathrm{d}\mathbf{x}, \quad \mathbf{K}_1 = D^* \int_S \nabla^2\mathbf{\Psi}\nabla^2\mathbf{\Psi}^\top \, \mathrm{d}\mathbf{x}, \quad \mathbf{K}_2 = h\alpha M_f \int_S \nabla^2\mathbf{\Psi}\mathbf{\Psi}^\top \, \mathrm{d}\mathbf{x}. \end{aligned} \tag{9}$$

The vector $\mathbf{F}_{\text{ext}}(t) = \mathbf{\Psi}(\mathbf{x}_0)\exp(j\omega t)$ collects the modal contributions of a harmonic excitation of amplitude F_{ext} and angular frequency ω applied at the point $\mathbf{x}_0 = (x_0, y_0)$. If the plate is excited acoustically by a plane wave of amplitude P_0, the pressure $\mathbf{p}(\mathbf{x}, t)$ applied to the fluid–solid mixture and the pressure difference within the fluid are assumed to be uniformly distributed. The corresponding discrete version is described by $\mathbf{P}_1 = 2P_0\mathbf{H}$ and $\mathbf{P}_2 = \phi_0 P_0 \mathbf{H}$ where

$$\mathbf{H} = \frac{\displaystyle\int_S \mathbf{\Psi}(\mathbf{x}) \, \mathrm{d}\mathbf{x}}{\displaystyle\int_S \mathbf{\Psi}(\mathbf{x}) \odot \mathbf{\Psi}(\mathbf{x}) \, \mathrm{d}\mathbf{x}} \tag{10}$$

represents the projection of the uniform pressure onto the modal basis with $\odot$, the element-wise (Hadamard) product. For a purely mechanical excitation, $\mathbf{P}_1$ and $\mathbf{P}_2$ vanish, whereas for a purely acoustic excitation, $\mathbf{F}_{\text{ext}}$ vanishes.

As a first step, a modal analysis is performed on Equation (7) by setting $\mathbf{Q}(t) = \mathbf{0}$. The resulting eigenvalue problem yields 3N eigenvalues, which naturally fall into three families: two sets of complex conjugate pairs associated with the structural displacement, and one set of purely real eigenvalues related to the relative fluid–solid displacement. The real eigenvalue corresponds to the natural frequency of the

[2] For a rectangular plate, $\Psi_{mn}(x, y) = \phi_m(x)\phi_n(y)$ where $\phi_k(\xi) = A_k \cosh \Omega_k \xi + B_k \cos \Omega_k \xi + C_k \sinh \Omega_k \xi + D_k \sin \Omega_k \xi$.

fluid–structure interaction governed by the local visco-thermal behavior inside the perforations. It remains constant across structural modes because it is determined by the fluid dynamics in the perforations, independently of the global structural response. The second step consists in computing the forced frequency response. The governing equations are projected onto the modal basis obtained from the preceding eigen-analysis, yielding a set of decoupled equations. These can be solved efficiently to obtain the steady-state response for each mode. Detailed expressions and the solution procedure can be found in [2, Section 3.2]. The displacement fields w_s and w obtained from the above resolution procedure serve as input to the acoustic radiation model developed in the following section.

2.3. Fluid loading and acoustic radiation impedance

The displacement fields obtained in Section 2.1 drive the acoustic radiation of the baffled MPP into the two surrounding semi-infinite fluid domains. Since the MPP radiates into an external fluid, the resulting fluid loading must be incorporated into the governing equations through an additional coupling term [32]. Since the perforation spacing is much smaller than the acoustic wavelength in air, the homogenized MPP radiates as an equivalent continuous plate. The acoustic radiation impedance of classical plate theory can be applied to the solid displacement field only, as the radiation from the dragged fluid mass is already accounted for through the tortuosity correction in Equation (4). For a baffled plate (i.e., a plate mounted in an infinite rigid baffle), the fluid loading is introduced into the governing equations by the addition of a coupling term dependent on the solid displacement $w_\mathrm{s}(\mathbf{x},t)$. Using the modal representation of $w_\mathrm{s}(\mathbf{x},t)$ given in Equation (6), the associated acoustic source term, which involves the acoustic radiation impedance, is expressed as

$$q_i(\mathbf{x},t) = -j\omega \sum_{k=1}^{\infty} Z_{ik}(\omega)(1-\phi_0) w_k^\mathrm{s}(t) \Psi_k(\mathbf{x}), \tag{11}$$

where the entries of the acoustic radiation impedance matrix read

$$Z_{ik}(\omega) = j\omega\rho_\mathrm{f} \int_S \int_{S_1} \Psi_i(\mathbf{x})\, G(\mathbf{x},\mathbf{x}_1)\, \Psi_k(\mathbf{x}_1)\, \mathrm{d}\mathbf{x}_1\, \mathrm{d}\mathbf{x}, \qquad k \equiv (p,q),\ p,q \geq 1, \tag{12}$$

where k denotes the pair (p,q) associated with the plate mode Ψ_{pq}. Under the light-fluid assumption, the acoustic radiation impedance matrix becomes diagonal, *i.e.* $Z_{ik}(\omega) = 0$ if $i \neq k$. Equation (12) involves the positions $\mathbf{x}$ of a transmitting element and $\mathbf{x}_1$ of a receiving element. In Equation (12), the Green function is defined for a half-space as

$$G(\mathbf{x},\mathbf{x}_1) = \frac{\exp(-jk_0\,\|\mathbf{x}-\mathbf{x}_1\|)}{2\pi\,\|\mathbf{x}-\mathbf{x}_1\|} \quad \text{with} \quad k_0 = \frac{\omega}{c_0}. \tag{13}$$

The operator $\|\cdot\|$ is the Euclidean norm and c_0 is the fluid celerity. In the present formulation, the Green's function corresponds to the acoustic field radiated by a point source in a baffled configuration.

2.4. Vibroacoustic indicators

In the vibroacoustic analysis of MPP, two distinct contributions to sound radiation, presented in Figure 2, can be identified: i) radiation from the solid plate characterized by the solid velocity v_s and ii) radiation from the perforation network, which behaves as an array of fluid pistons characterized by the fluid velocity v_f. The relative importance of these two contributions depends critically on the ratio between the viscous

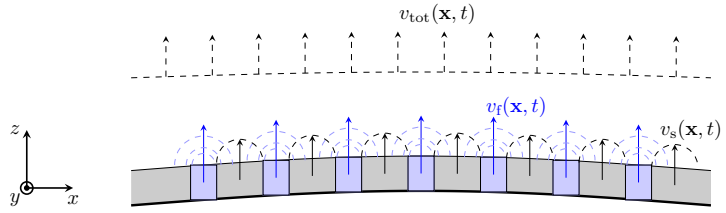

Figure 2: Velocities in the microperforated plate model.

boundary layer thickness and the perforation diameter. When perforations are very small, the fluid motion through the perforations is restricted by the limited aperture size, rendering the fluid's contribution to radiation negligible. Conversely, for large perforation ratios—where the diameter greatly exceeds the boundary layer thickness—the fluid is no longer effectively driven by the plate motion, and radiation from fluid pistons becomes negligible. Radiation from fluid pistons is only significant in the intermediate regime

where the boundary layer thickness is comparable to the perforation diameter, ensuring effective dragging of the fluid by the plate motion. Since this condition is fulfilled in the present study, the vibroacoustic analysis must account for radiation stemming from both the fluid and the solid, and the total acoustic particle velocity v_{tot} at the fluid–panel interface is therefore the relevant quantity to characterize this combined radiation. Following Takahashi and Tanaka [13], the average acoustic particle velocity v_{tot} at the fluid–panel interface is obtained by applying mass continuity to a control volume. At any point on the surface ($z = \pm h/2$), the volumetric flux consists of contributions from both the solid surface ($1 - \phi_0$) and the fluid passing through the perforations (ϕ_0). The mean particle velocity is therefore given by [13, 38]

$$S_{\mathrm{tot}} v_{\mathrm{tot}}(\mathbf{x}, t) = S_{\mathrm{s}} v_{\mathrm{s}}(\mathbf{x}, t) + S_{\mathrm{perf}} v_{\mathrm{f}}(\mathbf{x}, t) \quad \Rightarrow \quad v_{\mathrm{tot}}(\mathbf{x}, t) = (1 - \phi_0) v_{\mathrm{s}}(\mathbf{x}, t) + \phi_0 v_{\mathrm{f}}(\mathbf{x}, t), \tag{14}$$

where S_{tot}, S_{s}, and S_{perf} are the total panel area, the effective solid area, and the total perforation area, respectively, with $\phi_0 = S_{\mathrm{perf}}/S_{\mathrm{tot}}$. Equation (14) can also be written for displacement instead of velocity and reads $w_{\mathrm{tot}}(\mathbf{x}, t) = w_{\mathrm{s}}(\mathbf{x}, t) + w(\mathbf{x}, t)$. To characterize the coupled vibroacoustic behavior of the baffled MPP, three fundamental indicators are introduced according to [33]:

Radiated sound power quantifies the total acoustic energy emitted by the front surface of the MPP into the surrounding semi-infinite fluid domain, defined as the integration of sound intensity over the plate surface over a period of time:

$$W(\omega) = \frac{\omega}{2\pi} \int_0^{\frac{2\pi}{\omega}} \int_S P(\mathbf{x}, t) v_{\mathrm{tot}}(\mathbf{x}, t) \, \mathrm{d}\mathbf{x} \, \mathrm{d}t, \tag{15}$$

where the acoustic pressure field $P(\mathbf{x}, t)$ is obtained from the Rayleigh integral

$$P(\mathbf{x}, t) = -\rho_{\mathrm{f}} \omega^2 \int_{S_1} w_{\mathrm{tot}}(\mathbf{x}_1, t) G(\mathbf{x}, \mathbf{x}_1) \, \mathrm{d}\mathbf{x}_1. \tag{16}$$

This metric reflects the direct contribution of the structural vibrations and the acoustic flow through the perforations to the sound field.

Mean square velocity measures the space–time average of the squared total surface velocity of the plate, thus providing a global descriptor of its dynamic response amplitude. It is defined as

$$V^2(\omega) = \frac{\omega}{2\pi L_x L_y} \int_0^{\frac{2\pi}{\omega}} \int_S |v_{\mathrm{tot}}(\mathbf{x}, t)|^2 \, \mathrm{d}\mathbf{x} \, \mathrm{d}t. \tag{17}$$

Radiation efficiency expresses the fraction of the plate's vibrational energy that is effectively converted into radiated sound energy. It is obtained as the ratio of radiated acoustic power to the product of the mean square velocity, the plate surface area, and the characteristic acoustic impedance of the surrounding medium:

$$s(\omega) = \frac{W(\omega)}{\rho_{\mathrm{f}} c_0 V^2(\omega) L_x L_y}. \tag{18}$$

This dimensionless quantity, bounded between 0 and 1 for subsonic plate vibrations, serves as a direct indicator of the effectiveness of vibration-to-sound conversion.

For perforation diameters of the order of the thickness of the viscous boundary layers, the increase in flow rate as the fluid passes through the perforations during motion leads to a fluid velocity inside the perforations that is much larger than that of the solid. This velocity makes a non-negligible contribution to $\dot{w}_{\mathrm{tot}}$ and is discussed in Section 3.

3. Sensitivity analysis

In this section, the plate has dimensions 490 mm × 570 mm × 1 mm and is made of aluminum with $E = 66\,\mathrm{GPa}$ and $\rho_{\mathrm{s}} = 2680\,\mathrm{kg\,m^{-3}}$. The perforation diameter is such that the characteristic frequency (5) coincides with the natural frequency of the first mode of the perforated plate. The perforation ratio is set to 10 % and the structural damping, to $\eta_{\mathrm{s}} = 10^{-4}$.

3.1. Sensitivity of the MPP forced response to fluid load

The mean square velocity, the radiated acoustic power, and the radiation efficiency are computed from the displacement field of the equivalent solid plate as well as from that of the virtual fluid plate, obtained after resolution of Equation (1) for a purely mechanical excitation. The mean square velocity and the radiated acoustic power are obtained using six modal functions in each spatial direction, resulting in $N = 36$ degrees-of-freedom to ensure convergence.

The perforation diameter $d = 1.4\,\text{mm}$ is chosen to maximize the added viscous damping on the first plate mode, such that $f_c \approx f_1 = 18.4$ Hz. Figure 3(a) shows the mean square velocity of the MPP and Figure 3(b), the radiated acoustic power, both as a function of the driving frequency. Two MPPs are compared: (i) an air-saturated MPP and (ii) an MPP filled with a virtual fluid with zero dynamic viscosity, in order to isolate the contribution of visco-thermal dissipation. In Figure 3, it is noteworthy that these

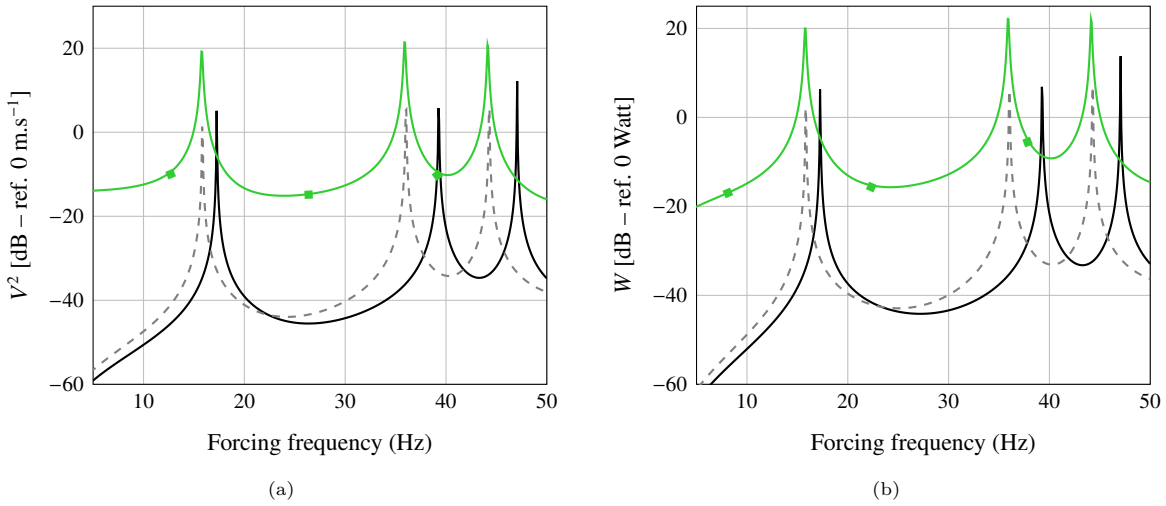

Figure 3: Vibroacoustic indicators for an MPP: (a) total mean square velocity; (b) radiated sound power. A non perforated plate (——) is compared to two MPP with fixed perforation ratio: (—■—) saturated by a fluid with a dynamic viscosity of 1.84×10^{-5} Pa s; (- - -) saturated by a virtual fluid with zero dynamic viscosity.

MPP vibroacoustic indicators appear higher than those of the solid plate alone, and even higher than those of the MPP saturated by a non-viscous fluid. This apparent increase results from the interplay between two competing mechanisms: viscous damping within the perforations, which decreases vibration amplitude, and the motion of oscillating fluid columns. These columns function as a distributed array of acoustic 'air pistons'. When the viscous boundary layer becomes comparable to the perforation diameter, fluid-borne radiation effectively supersedes solid-phase damping losses. Consequently, the total radiated power (and the total mean square velocity) may exceed not only that of the solid plate alone, but also that of the non-viscous case. In the latter, the permeable structure exhibits lower radiation efficiency due to a reduced effective radiating area, as shown in Section 3.2. This observation can also be made in Figure 4, which presents the mean square velocity and the radiated sound power for four values of the perforation ratio: $\phi_0 = 0\,\%$, $5\,\%$, $10\,\%$, and $15\,\%$. The case with $\phi_0 = 0\,\%$ corresponds to a non-perforated plate. While structural damping increases with the perforation ratio, a higher ratio also allows more fluid to participate in structural radiation. Consequently, both the mean square velocity and the radiated acoustic power increase with ϕ_0. Indeed, for a baffled plate, the perforations act as additional radiating elements rather than paths for acoustic short-circuiting [1]. The apparent increase in radiated power with perforation ratio arises from the contribution of oscillating fluid within the perforations. Due to flow continuity, the fluid velocity $v_f \approx v_s/\phi_0$ in the perforations can significantly exceed the plate velocity [13]. Although this fluid motion contributes to the total radiated power, the radiation efficiency is expected to decrease due to the acoustic short-circuit effect inherent to the fluid permeability and the reduced effective radiating surface [1][3]. This explains why perforated plates can simultaneously exhibit higher total radiated power yet lower radiation efficiency compared to their non-perforated counterparts. These effects are only observable when the perforation diameter is of the same order as the viscous boundary layer thickness δ_v. For $\phi = 10\,\%$, Figure 5 highlights the fluid contribution to the radiated acoustic power by comparing three MPP configurations with different perforation diameters: $d \ll \delta_v$, $d \approx \delta_v$, and $d \gg \delta_v$.

[3]This is demonstrated by the comparison between viscous and non-viscous MPP in Section 3.2, where the introduction of viscous losses leads to a reduction in the amplitude of vibrations around the characteristic frequency f_c.

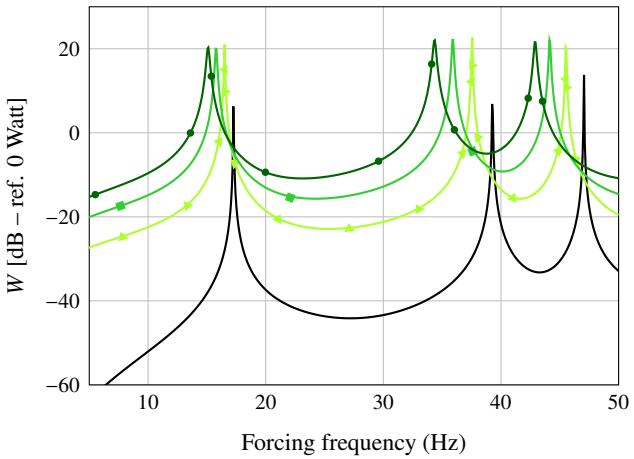

Figure 4: Radiated sound power for four values of ϕ_0: (——) $\phi_0 = 0\,\%$, corresponding to the non-perforated reference plate; (—▲—) $\phi_0 = 5\,\%$; (—■—) $\phi_0 = 10\,\%$; and (—●—) $\phi_0 = 15\,\%$.

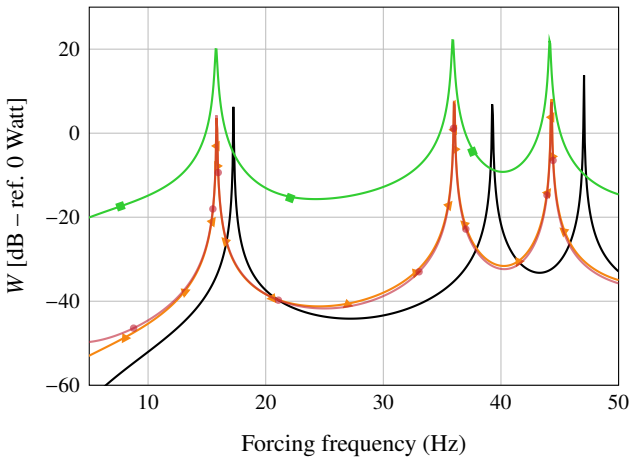

Figure 5: Radiated sound power for the reference solid plate (——) and three MPP with different perforation diameters for a constant ϕ, $d \ll \delta_\mathrm{v}$ (—▲—), $d \approx \delta_\mathrm{v}$ (—■—) and $d \gg \delta_\mathrm{v}$ (—●—), illustrating that a significant fluid-borne radiation contribution arises only when the hole diameter is of the order of the viscous boundary layer thickness.

Two main trends can be observed: i) for very small perforations compared to δ_v, the flow resistivity is too high, limiting the fluid motion within the holes; ii) for large perforations comparable to δ_v, the fluid is not sufficiently driven by the thin boundary layers, and its participation in sound radiation becomes negligible. In both limiting cases, the fluid contribution to radiation is minimal, and the observed reduction in acoustic power mainly results from the plate's increased permeability and reduced radiating surface area.

3.2. Sensitivity of the MPP acoustic radiation efficiency to perforation ratio

The radiation efficiency offers a global insight into the vibroacoustic behavior of a structure. Accordingly, the present section investigates the radiation efficiency with respect to the excitation frequency for plates simply supported on all edges, with dimensions 490 mm × 570 mm × 1 mm. In order to quantify the contribution of each domain (fluid and solid) and thus assess the contribution of the added viscous damping to the overall radiation of the MPP, three cases are considered:

1) a non-perforated reference plate;
2) an equivalent MPP with a non-viscous fluid in the perforations, i.e., without added damping – this case is modeled by setting η_f to zero;
3) a MPP saturated with air, accounting for the coupling between the fluid and the structure.

The perforation ratio is set to 10 %, and the hole diameter is chosen as $d = 1.4$ mm in order to maximize the added viscous damping on the first plate mode, such that $f_\mathrm{c} \approx f_1 = 18.4$ Hz, where f_c is the characteristic frequency defined in Equation (5). Comparison shows that the radiation efficiency of the MPP is significantly reduced compared to that of the non-perforated plate around the first structural resonance. Comparison with a non-viscous fluid in the perforations suggests that both the acoustic short-circuit effect and the reduction of the radiating surface contribute to a decrease in the acoustic

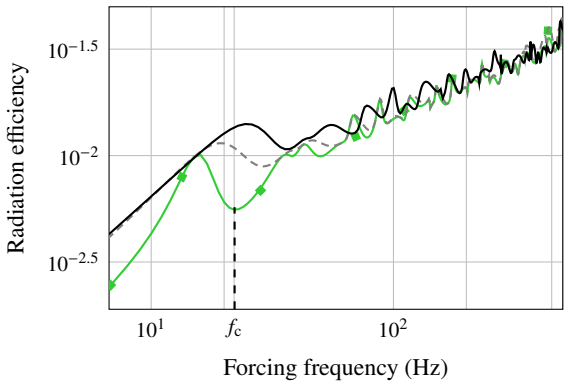

Figure 6: Radiation efficiency as a function of the excitation frequency for three mechanically excited plates: (——) the non-perforated reference plate; (- - -) the MPP without fluid in the perforations; and (—■—) the MPP saturated with air. The plate dimensions are 490 mm × 570 mm × 1 mm, with all edges simply supported. The perforations are designed to maximize damping around the first resonance frequency of the MPP, with $d = 1.4$ mm and $\phi_0 = 10\%$.

radiation efficiency. It should be noted, however, that both the density and Young's modulus values are affected [36], which may also contribute to the reduction of the radiation efficiency. Furthermore, at low frequencies, the drop in radiation efficiency is mainly related to the large acoustic wavelength compared to the structural dimensions. In this regime, the plate motion produces only a weak pressure difference in the surrounding fluid, which reduces the net radiated pressure and limits the efficiency of the radiation process. Even though the plate is baffled, the presence of perforations still tends to facilitate fluid communication through the structure, which further contributes to the reduction of radiation efficiency in the low-frequency range. The only difference between the both MPP is the consideration of the viscous dissipation into microperforations in the case of non-zero dynamic viscosity. When losses are introduced in the perforations, the radiation efficiency decreases further. Part of the vibrational energy of the plate is dissipated within the perforations through viscous and thermal effects, rather than being converted into acoustic radiation. As a result, the effective coupling between the plate motion and the surrounding fluid is reduced, leading to a lower radiation efficiency. As a result, although both the radiated power and the mean square velocity decrease due to viscous dissipation within the perforations, the radiation efficiency around $f \equiv f_c$ also decreases. This indicates that the radiated power diminishes more rapidly than the vibrational energy, which can be attributed to the acoustic short-circuit effect, the reduction of the effective radiating surface, and the downward frequency shift of the first mode.

3.3. Nonuniform distribution of perforations

From a mechanical point of view, perforating a plate usually reduces its flexural rigidity and natural frequencies, decreases the structure's overall fatigue resistance and can cause localized stress concentrations around the holes. To mitigate these undesirable effects while retaining the beneficial effects of the perforations, the latter were only distributed in certain areas of the plate. The spatial distribution of perforations also affects the magnitude of the added damping [3]. For a given mode, perforations located near regions of maximum displacement generate greater damping. This effect arises from viscous friction within the boundary layers of the MPP, which increases with the relative velocity between the fluid and the structure. Accordingly, the added damping can be maximized by concentrating the perforations at the antinodes of the modes whose amplitudes are intended to be reduced. As the additional damping introduced by the micro-perforations is particularly significant in the low-frequency range [2], the perforations were concentrated in the centre of the plate (i.e. the displacement belly of the first mode of a plate supported on all its edges).

To study the impact of perforation distribution on radiation efficiency, a spatial heterogeneity is introduced into the analytical model. The perforation ratio is now spatially dependent and is thus expressed in terms of a distribution function:

$$\phi(x, y) = \phi_0^{(0)} \mathrm{Ih}(x, y), \tag{19}$$

where $\mathrm{Ih}(x, y)$ is a normalized inhomogeneity function, and ϕ_0 denotes the maximum perforation ratio, corresponding to $\max_{(x,y)} \mathrm{Ih}(x, y) = 1$. Since all the terms involving ϕ_0 are now functions of space, the spatial projections introduced in Equation (9) must be reformulated to account for this spatial dependence[4]. Once solved, the relative solid and fluid-solid displacement fields serve as inputs for

[4]For more details regarding the spatial projection and the resolution procedure, the reader is referred to [3, Section 4.1].

calculating radiation efficiency via Equation (18). Figure 7(a) shows the overall radiated efficiency for three plates: a non-perforated reference plate, an MPP with $\mathrm{Ih}(x, y) = 1$ and an MPP with

$$\mathrm{Ih}(x, y) = \Pi(x, y) = \begin{cases} 1 & \text{if} \quad \frac{1}{3} \leq \frac{x}{L_x} \leq \frac{2}{3}, \\ 0 & \text{else.} \end{cases} \tag{20}$$

The absolute difference in radiation efficiency remains below 1 %, even though the overall perforation ratio decreases from 10 % to 5 % due to the modification introduced by Equation (20). Keeping perforations

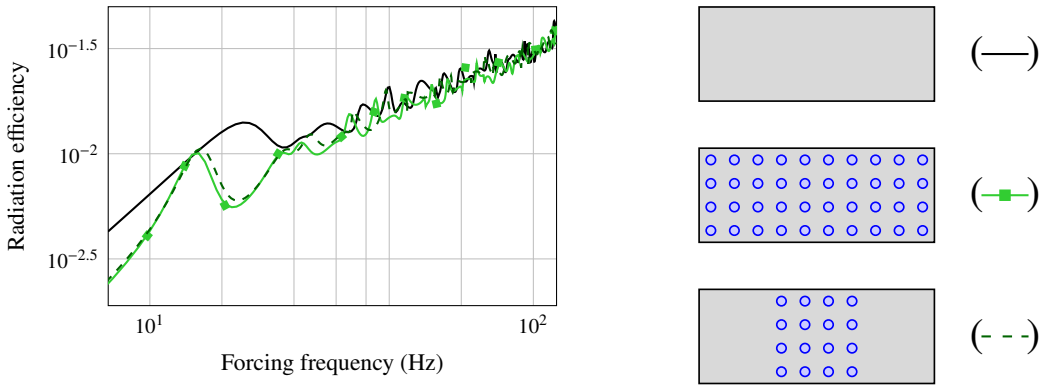

Figure 7: In (a), the overall acoustic radiation efficiency for the three cases represented in (b): (——) the non-perforated reference plate; (—■—) the MPP with $\mathrm{Ih}(x, y) = 1$ and (- - -) the MPP with $\mathrm{Ih}(x, y)$ defined according to Equation (20).

only in the central region (i) limits the mechanical drawbacks associated with reduced stiffness and fatigue over the entire structure; and (ii) reduces the low-frequency radiation efficiency of the MPP.

4. Numerical validation

4.1. Numerical modeling

In this section, we employ a finite element approach to study the MPP's radiation and validate the analytical model. Thermal and viscous losses occurring within the boundary layers near the walls are taken into account by solving the thermo-viscous problem equations, which correspond to the linearized Navier-Stokes equations coupled with energy conservation. These equations are implemented in COMSOL Multiphysics™ using the ThermoViscous Acoustics (TVA) module, enabling the simulation of visco-thermal effects in confined fluid domains [39]. The thermoviscous acoustic formulation captures acoustic perturbations of pressure, velocity, and temperature fields, thus accurately modeling dissipative phenomena at the fluid-solid interface.

To validate the analytical model, an MPP mounted in a baffle and separates two semi-infinite fluid domains is considered, see Figure 8. The acoustic loading from the external fluid is taken into account by explicitly modeling these surrounding fluid domains. The MPP being immersed in an infinite fluid, the far-field impedance conditions $Z_0 = \rho_\mathrm{f} c_0$ are applied on both sides of the fluid domain. Far away from the structure, the radiated field becomes a plane wave with nearly normal incidence, which justifies the use of the characteristic impedance. This point is further discussed in Section 5. The structure is clamped at the abscissa $x = 0$ and a mechanical point forcing $f_\mathrm{ext}(\mathbf{x}_0, t)$ with $F_\mathrm{ext} = 1\,\mathrm{N}$ is applied at $x_0 = 115.65\,\mathrm{mm}$ and $y_0 = L_y/2$. Other relevant parameters are indicated in Table 1. The perforation

Microperforated plate		**Mechanical parameter (solid/fluid)**	
L_x (mm)	131	ρ_s ($\mathrm{kg\,m^{-3}}$)	7850
L_y (mm)	30.7	ρ_f ($\mathrm{kg\,m^{-3}}$)	1.213
h (mm)	1.0	E (GPa)	203
ϕ_0 (%)	10	ν	0.3
d (mm)	1	η_s	10^{-4}

Table 1: Numerical values implemented for the finite elements modeling.

ratio is set to $\phi_0 = 10\,\%$ and $d = 1\,\mathrm{mm}$ is chosen to maximize the added damping around 50 Hz.

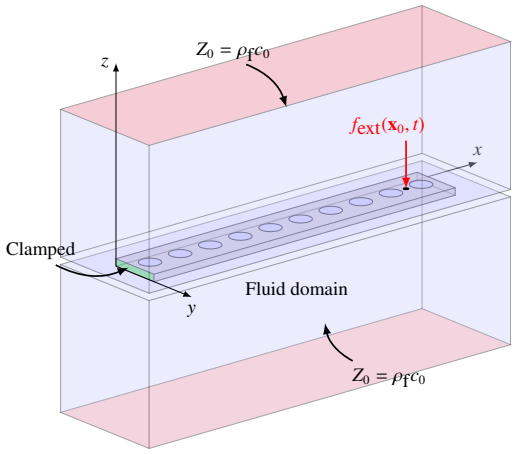

Figure 8: Clamped MPP with dimensions 131 mm × 30.7 mm × 1 mm. The MPP is fixed at the point of abscissa $x = 0$ and mechanically excited at position $\mathbf{x}_0 = (x_0, y_0)$. The perforation diameter $d = 1$ mm is chosen to maximize damping of the first mode, with a perforation ratio $\phi_0 = 10$ %. The far field is modeled by applying impedance Z_0 on both sides of the fluid domain. Visco-thermal losses in the perforations are modeled using the TVA approach.

To reduce computational cost, the plate is assumed to be much longer than it is wide, and only a single row of perforations is considered. The model is therefore simplified using the Euler–Bernoulli beam theory. Thus, it is possible to adjust the width of the MPP to obtain $\phi_0 = 10\,\%$ for a single row of perforations, leading to

$$L_y = \frac{\pi d^2}{4\phi_0 L_x}. \tag{21}$$

The finite element model is solved over the frequency range from 10 Hz to 90 Hz, using a frequency step of 5 Hz. To accurately capture the system's response near resonance, the frequency resolution is refined to 0.5 Hz in the vicinity of the peak response. Since the analytical model is based on a homogenized representation of the MPP, the radiated acoustic pressure is evaluated numerically at a distance sufficiently far from the perforations[5] in order to guarantee meaningful comparison with the theoretical predictions. Indeed, the local acoustic radiation generated near the perforations first evolves into a cylindrical wave at intermediate distances, and eventually transitions into a planar wave in the far field. Note that, in our study, the thermo-viscous boundary layers are indeed modeled as confined within a rigid-walled duct. This assumption is fully justified for the frequency range under consideration, since it remains below the duct's first cutoff frequency. In this regime, only the plane mode is propagative, and the lateral boundary conditions have no influence on the response.

4.2. Numerical and analytical results

Figure 9 presents the numerical results. Figure 9(a) and Figure 9(b) compare the analytically and FEM-obtained mean square velocity and radiation sound power for the fluid-saturated MPP. The mean square velocity from FEM is computed by integrating the acoustic velocity over the perforation surfaces and the solid velocity over the plate surface. Unlike the mean square velocity, the radiated acoustic power requires particular care regarding the observation distance: in the immediate vicinity of the perforations, the acoustic field is dominated by evanescent contributions at the scale of the perforation array, which decay rapidly with distance[6]. The radiated pressure is therefore evaluated numerically at the outer boundaries of the fluid domain, at a distance from the plate that is sufficiently large to ensure a quasi-planar flow, in accordance with the homogenised model assumptions. The comparison between the analytical model and the FEM in Figures 9(a) and 9(b) confirms the validity of the analytical model proposed in Section 4.

Based on the mean square velocity and the radiated acoustic power obtained via FEM, the radiation efficiency from simulation can be compared with its analytical counterpart. Accordingly, Figure 9(c) presents the radiation factor obtained analytically for the MPP characterized in Table 1, as well as for a non-perforated plate. For computational efficiency, the FEM-based radiation factor in Figure 9(c) is provided only for selected frequencies between 40 Hz and 5000 Hz.

[5] Further information on the near field/far field transition distance criterion is provided in Section 5.
[6] The spatial scales governing this near-to-far-field transition are discussed in Section 5.

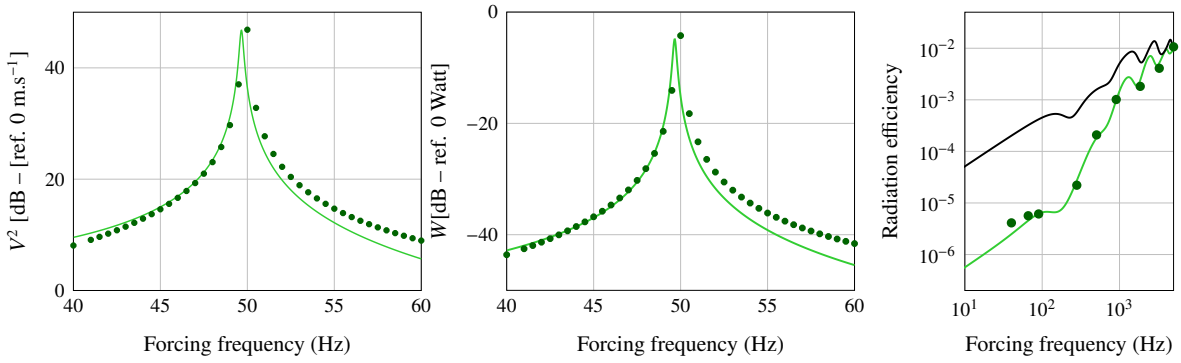

(a) (b) (c)

Figure 9: Numerical validation of the analytical model against FEM results: (a) mean square velocity; (b) radiated sound power and (c) radiation efficiency, for the proposed analytical model (——) and for the FEM (●). MPP properties given in Table 1. The reference case (——) is also provided in (c).

5. Spatial scales of acoustic radiation

In an MPP subjected to structural excitation, the acoustic field arises from the superposition of three mechanisms: i) piston-type radiation from the oscillatory flow inside each perforation, ii) elastic radiation from the vibrating plate, and iii) collective effects imposed by the periodic arrangement of holes. Near an individual aperture, the oscillatory flow produces a reactive field governed by the effective diameter

$$d_{\text{eff}} = d - 2\delta_{\text{v}}, \quad \delta_{\text{v}} = \sqrt{\frac{2\mu_{\text{f}}}{\omega\rho_{\text{f}}}} \tag{22}$$

with decay length [40, 41]

$$r_{\text{R}} = \frac{d_{\text{eff}}^2}{2\lambda} \tag{23}$$

corresponding to the Rayleigh distance with λ the wave length. Periodic arrays also generate evanescent network modes governed by the evanescent Floquet–Bloch harmonics [42, 43]. For an MPP, the network consists of a periodic repetition of circular perforations arranged in either a rectangular or square pattern. The unit cell is defined by the center-to-center spacing of the circular perforations: a along the x-axis and b along the y-axis, see Figure 10. Each perforation is modeled as a circular hole of radius r. The radiating element thus has an area of $\mathscr{A} = ab - s_{\text{p}}$, with s_{p} the aperture area. This radiating element is assumed to be equivalent to a square radiating element of identical area, with a side length $p = \sqrt{ab - s_{\text{p}}}$.

For a perforated structure, the length correction proposed in [9] can be interpreted in terms of evanescent transverse modes [44]. The acoustic field in the direction normal to the plate results from the superposition of the main propagation mode $(m, n) = (0, 0)$ and an infinite number of evanescent modes associated with the harmonics of the array. According to the field theory of guided waves [45], each mode (m, n) has an axial wave number

$$k_{z,mn} = \sqrt{k_0^2 - k_{x,m}^2 - k_{y,n}^2} \qquad \text{with} \quad k_{x,m} = \frac{2\pi m}{p}, \quad k_{y,n} = \frac{2\pi n}{p} \quad \text{and} \quad k_0 = \frac{2\pi}{\lambda} \tag{24}$$

whose value determines the attenuation velocity in the normal direction. All orders satisfying $k_{x,m}^2 + k_{y,n}^2 > k_0^2$ are evanescent. Their decay length is $\ell_{\text{ev}} = k_{\text{ev}}/2\pi$ with $k_{\text{ev}} = 1/\text{Im}(k_{z,mn})$ which reads, in the general case,

$$k_{\text{ev}} = \frac{1}{\sqrt{\dfrac{m^2 + n^2}{\mathscr{A}} - \left(\dfrac{k_0}{2\pi}\right)^2}} \tag{25}$$

By using the low-frequency assumption $k_0^2 \ll k_{x,m}^2 + k_{y,n}^2$ and assuming that the $(1, 0)$ and $(0, 1)$ harmonics have the smallest nonzero transverse wavenumbers and therefore dominate the near field, it follows that $\ell_{\text{ev}} \simeq \frac{\sqrt{\mathscr{A}}}{2\pi}$. Since ℓ_{ev} is real, $\mathscr{A}$ must be real and the perforation area must remain smaller than the unit-cell area. For the particular case of a circular perforation within a rectangular unit cell, see Figure 10(b), the general expression in Equation (25) can be simplified by substituting the perforation area with $s_{\text{p}} = \pi r^2$. Applying the same low-frequency and near-field assumptions then yields

$$\ell_{\text{ev}} \simeq \frac{\sqrt{ab}}{2\pi}\sqrt{1 - \frac{\pi r^2}{ab}}, \quad \ell_{\text{ev}} \in \mathbb{R}^+, \quad \forall\, r < \frac{ab}{\pi}. \tag{26}$$

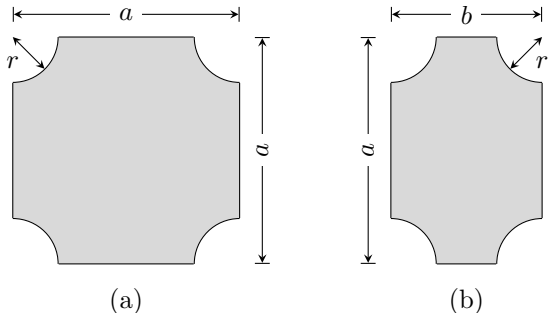

Figure 10: Unit cell, defined by the center-to-center spacing of the circular perforations: (a) a circular array and (b) a rectangular array.

In the case of a micro-perforated plate with viscous dissipation, the perforation radius must be adjusted to compensate for the reduction caused by viscous boundary layers and becomes $r_{\text{eff}} = r - \delta_{\text{v}}$ and the wave number become complex according to [46]. Visco-thermal losses affect the real part of the modal impedance by slightly reducing the extension of the evanescent field. It is observed that the area ab of the elementary cell ($s_{\text{c}} = ab$) and that of the perforation ($s_{\text{p}} = \pi r^2$) appear in Equation (26), which can therefore be written in the form

$$\ell_{\text{ev}} \simeq \frac{\sqrt{s_{\text{c}}}}{2\pi}\sqrt{1 - \frac{s_{\text{p}}}{s_{\text{c}}}}, \quad \ell_{\text{ev}} \in \mathbb{R}^+, \quad \forall\, s_{\text{p}} < s_{\text{c}}. \tag{27}$$

In practice, the transition distance to the far field is set at $r_{\text{ev}} = 3\ell_{\text{ev}}$ which ensures that the amplitude of the dominant evanescent mode is attenuated by a factor greater than 20, making its contribution negligible compared to that of the propagating mode.

Beyond the evanescent region, the radiated field enters the Fraunhofer regime, characterized by the Fraunhofer distance

$$r_{\text{F}} = \frac{2L_{\text{eff}}^2}{\lambda}, \tag{28}$$

where L_{eff} is the largest dimension of the radiation surface.

The MPP radiation pattern arises from a hierarchy of spatial scales: perforation-scale reactive fields, a lattice-controlled near-field including evanescent contributions, and far-field diffraction governed by the overall structure. For illustration purposes, the MPP for which the geometric parameters are given in Table 1 is used to calculate the different lengths at $f = 50\,\text{Hz}$. The results are stored in Table 2 and illustrated in Figure 11, which shows the acoustic velocity and pressure fields obtained near the perforations. According to Table 2, mechanisms relating to the acoustic radiation field at the hole aperture is negligible. The near field of the MPP is governed by the perforation spacing, which controls the strength

Characteristic distance	Numerical values
r_{R}	0.17 µm
ℓ_{ev}	0.45 mm
r_{F}	4.95 mm

Table 2: Characteristic distances, calculated at $f = 50\,\text{Hz}$ from Equations (23), (26) and (28) reported for a MPP immersed in air, with geometric parameters specified in Table 1.

of evanescent modes and their coupling to the far-field radiation. Overall, the near/far transition is determined by the plate size and the perforation spacing, while the perforation diameter primarily affects the extent of the local near field, the validity of the homogenization approach, and viscous losses. As our model is homogenized, meaningful comparisons with numerical simulations can only be made at distances beyond r_{F}, where the homogenized description is valid.

6. Conclusion

The present paper extends the classical theory of plate acoustic radiation to the case of microperforated plate (MPP) saturated by a light fluid. The homogeneous fluid and solid vibration fields are obtained using the analytical model previously developed in [2]. Although the oscillating air within the perforations can contribute to the total radiated power, the overall efficiency of sound radiation decreases, it is analytically showed that, under mechanical excitation, the presence of microperforations leads to a marked

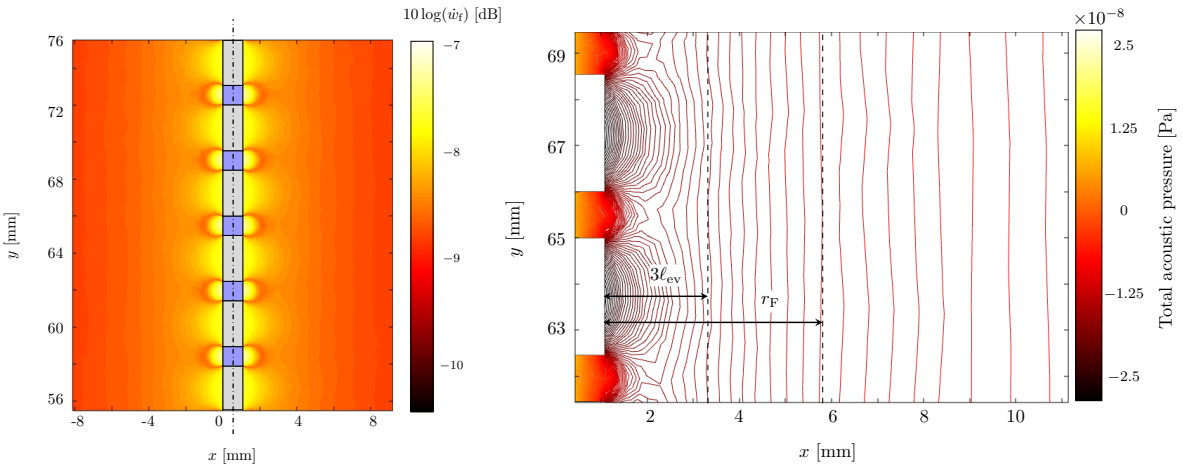

Figure 11: Results for the COMSOL simulation at $f = 50\,\text{Hz}$: (a) acoustic velocity field in dB; (b) acoustic pressure field around three perforations, in Pa. The characteristic lengths ℓ_{ev} and r_{F} are reported in (b).

reduction in the acoustic radiation efficiency of the structure. This reduction results from three competing mechanisms: (i) the acoustic short-circuit effect, (ii) the decrease in effective radiating surface area due to the perforations, and (iii) the reduction in vibration amplitude induced by the additional damping associated with visco-thermal dissipation within the perforations. Adjusting the perforation parameters can simultaneously reduce vibrations and radiated noise in a specific frequency band without adding mass. To validate the analytical predictions, a numerical model based on the finite element method is developed to solve the coupled elastic and thermo-visco-acoustic problem. The spacing of the perforations plays a key role in the formation of the MPP near field, as it governs both the amplitude of the evanescent modes and their coupling with the radiated field. The proposed homogenized model is valid beyond the Fraunhofer distance, where the radiated field approaches a quasi-plane wave behavior.

CRediT authorship contribution statement

Lucie Gallerand: Conceptualization, Methodology, Software, Validation, Writing - original draft, Writing - review & editing. **Mathias Legrand**: Conceptualization, Methodology, Supervision, Writing - original draft, review & editing. **Raymond Panneton**: Conceptualization, Methodology, Supervision, Writing - review & editing. **Philippe Leclaire**: Conceptualization, Methodology, Supervision, Writing - original draft, review & editing. **Thomas Dupont**: Conceptualization, Methodology, Supervision, Resources, Funding acquisition, Writing - original draft, review & editing.

References

[1] A. Putra and D.J. Thompson. Sound radiation from perforated plates. *Journal of Sound and Vibration*, 329(20):4227–4250, 2010. [DOI].

[2] L. Gallerand, M. Legrand, T. Dupont, and P. Leclaire. Vibration and damping analysis of a thin finite-size microperforated plate. *Journal of Sound and Vibration*, 541:117295, 2022. [DOI], [OA].

[3] L. Gallerand, M. Legrand, T. Dupont, R. Panneton, and P. Leclaire. Damping performance of finite microperforated plates using multi-size and spatial distributions of perforations. *Applied Acoustics*, 2024. [DOI], [OA].

[4] P. Cobo and F. Simón. Multiple-layer microperforated panels as sound absorbers in buildings: A review. *Buildings*, 9(2):53, 2019. [DOI].

[5] M. Mohammadi, M. Ishak, M. Hameed Sultan, and E. Zainudin. A Comprehensive Review of Factors Influencing the Sound Absorption Properties of Micro-Perforated Panel Structures. *Journal of Vibration Engineering & Technologies*, 13(5):319, 2025. [DOI].

[6] M.Q. Wu. Micro-perforated panels for duct silencing. *Noise Control Engineering Journal*, 45(2):69–77, 1997. [DOI], [OA].

[7] L. Wang and T. Wang. Investigation of the effect of perforated sheath on thermal-flow characteristics over a gas turbine reverse-flow combustor—Part 2: Computational analysis. *Journal of Thermal Science and Engineering Applications*, 12(4):041004, 2020. [DOI], [OA].

[8] D.-Y. Maa. Microperforated-panel wideband absorbers. *Noise Control Engineering Journal*, 29(3):77, 1987. [DOI], [OA].

[9] N. Atalla and F. Sgard. Modeling of perforated plates and screens using rigid frame porous models. *Journal of Sound and Vibration*, 303:195–208, 2007. [DOI], [OA].
[10] T. Dupont, G. Pavic, and B. Laulagnet. Acoustic properties of lightweight micro-perforated plate systems. *Acta Acustica united with Acustica*, 89(2):201–212, 2003. [OA].
[11] T. Bravo, C. Maury, and C. Pinhède. Vibroacoustic properties of thin micro-perforated panel absorbers. *Journal of the Acoustical Society of America*, 132:789–798, 2012. [DOI], [OA].
[12] J. Kang and H.V. Fuchs. Predicting the absorption of open weave textiles and micro-perforated membranes backed by an air space. *Journal of Sound and Vibration*, 220(5):905–920, 1999. [DOI].
[13] D. Takahashi and M. Tanaka. Flexural vibration of perforated plates and porous elastic materials under acoustic loading. *Journal of the Acoustical Society of America*, 112(4):1456–1464, 2002. [DOI], [OA].
[14] M.A. Biot. Theory of propagation of elastic waves in a fluid-saturated porous solid. I. Low-frequency range. *Journal of the Acoustical Society of America*, 28(2):168–178, 1956. [DOI], [OA].
[15] M.A. Biot. Theory of propagation of elastic waves in a fluid-saturated porous solid. II. Higher frequency range. *Journal of the Acoustical Society of America*, 28(2):179–191, 1956. [DOI], [OA].
[16] D.-Y. Maa. Potential of microperforated panel absorber. *Journal of the Acoustical Society of America*, 104:2861, 1997. [DOI], [OA].
[17] M. Toyoda and D. Takahashi. Reduction of acoustic radiation by impedance control with a perforated absorber system. *Journal of Sound and Vibration*, 286(3):601–614, 2005. [DOI].
[18] M. Toyoda, M. Tanaka, and D. Takahashi. Reduction of acoustic radiation by perforated board and honeycomb layer systems. *Applied Acoustics*, 68(1):71–85, 2007. [DOI].
[19] B. Laulagnet. Sound radiation by a simply supported unbaffled plate. *The Journal of the Acoustical Society of America*, 103(5):2451–2462, 1998. [DOI], [OA].
[20] Z. Zhu, Y. Song, Y. Zhang, Q. Liu, and G. Wang. Sound radiation of the plate with arbitrary holes. *International Journal of Mechanical Sciences*, 264:108814, 2024. [DOI].
[21] S. Xie, Z. Li, H. Yan, and S. Yang. Ultra-broadband sound absorption performance of a multi-cavity composite structure filled with polyurethane. *Applied Acoustics*, 189:108612, 2022. [DOI].
[22] Y.Y. Lee, E.W.M. Lee, and C.F. Ng. Sound absorption of a finite flexible micro-perforated panel backed by an air cavity. *Journal of Sound and Vibration*, 287:227–243, 2005. [DOI].
[23] Y.Y. Lee and E.W.M. Lee. Widening the sound absorption bandwidths of flexible micro-perforated curved absorbers using structural and acoustic resonances. *International Journal of Mechanical Sciences*, 49(8):925–934, 2007. [DOI].
[24] M. Toyoda, R.L. Mu, and D. Takahashi. Relationship between Helmholtz-resonance absorption and panel-type absorption in finite flexible microperforated-panel absorbers. *Applied Acoustics*, 71(4):315–320, 2010. [DOI].
[25] T. Bravo, C. Maury, and C. Pinhède. Sound absorption and transmission through flexible micro-perforated panels backed by an air layer and a thin plate. *Journal of the Acoustical Society of America*, 131:3853–3863, 2012. [DOI].
[26] J.S. Bell, I.R. Summers, A.R.J. Murray, E. Hendry, J.R. Sambles, and A.P. Hibbins. Low acoustic transmittance through a holey structure. *Physical Review B*, 85:214305, 2012. [DOI].
[27] T. Bravo, C. Maury, and C. Pinhède. Enhancing sound absorption and transmission through flexible multi-layer micro-perforated structures. *The Journal of the Acoustical Society of America*, 134(5):3663–3673, 2013. [DOI].
[28] C. Li, B. Cazzolato, and A. Zander. Acoustic impedance of micro perforated membranes: Velocity continuity condition at the perforation boundary. *Journal of the Acoustical Society of America*, 139(1):93–103, 2016. [DOI], [OA].
[29] J. Tournadre, M. A. Temiz, P. Martınez-Lera, W. De Roeck, and W. Desmet. Vibro-acoustic response of flexible micro-perforated plates: Impact of the boundary condition at the perforation walls. In *Proceedings of ISMA*, 2016.
[30] P. Leclaire, K.V. Horoshenkov, and A. Cummings. Transverse vibration of a thin rectangular porous plate saturated by a fluid. *Journal of Sound and Vibration*, 247(1):1–18, 2001. [DOI], [OA].
[31] L. Gallerand, M. Legrand, R. Panneton, P. Leclaire, and T. Dupont. Added nonlinear damping of homogenized fluid-saturated microperforated plates in forchheimer flow regime. *Journal of Sound and Vibration*, 606:119018, 2025. [DOI], [OA].
[32] H. Aygun, K. Attenborough, and A. Cummings. Predicted effects of fluid loading on the vibration of elastic porous plates. *Acta Acustica united with Acustica*, 93:6, 2007. [OA].
[33] O. Foin, J. Nicolas, and N. Atalla. An efficient tool for predicting the structural acoustic and vibration response of sandwich plates in light or heavy fluid. *Applied Acoustics*, 57(3):213–242, 1999. [DOI].
[34] H. Nélisse, O. Beslin, and J. Nicolas. A generalized approach for the acoustic radiation from a baffled or unbaffled plate with arbitrary boundary conditions, immersed in a light or heavy fluid. *Journal of Sound and Vibration*, 211(2):207–225, 1998. [DOI], [OA].
[35] R. Panneton and N. Atalla. Numerical prediction of sound transmission through finite multilayer systems with poroelastic materials. *The Journal of the Acoustical Society of America*, 100(1):346–354, 1996. [DOI], [OA].
[36] A.R. Boccaccini and Z. Fan. A new approach for the Young's modulus-porosity correlation of ceramic materials. *Ceramics International*, 23:239–245, 1997. [DOI], [OA].
[37] M.A. Biot and D.G. Willis. The elastic coefficients of the theory of consolidation. *Journal of Applied Mechanics*, pages 594–604, 1957. [DOI].

[38] H. Deresiewicz and R. Skalak. On uniqueness in dynamic poroelasticity. *Bulletin of the Seismological Society of America*, 53(4):783–788, 1963. [DOI].
[39] COMSOL. Comsol: Acoustic module user's guide, 2023. [URL].
[40] A. Pierce. *Acoustics: An Introduction to Its Physical Principles and Applications*. Springer International Publishing, Cham, 2019. [DOI].
[41] S. Laurens, E. Piot, A. Bendali, M'b Fares, and S. Tordeux. Effective conditions for the reflection of an acoustic wave by low-porosity perforated plates. *Journal of Fluid Mechanics*, 743:448–480, 2014. [DOI], [OA].
[42] C. Linton and P. Martin. Semi-infinite arrays of isotropic point scatterers. a unified approach. *SIAM Journal on Applied Mathematics*, 64(3):1035–1056, 2004. [DOI], [OA].
[43] Y. Zhou, M.-H. Lu, L. Feng, X. Ni, Y.-F. Chen, Y.-Y. Zhu, S.-N. Zhu, and N.-B. Ming. Acoustic surface evanescent wave and its dominant contribution to extraordinary acoustic transmission and collimation of sound. *Physical review letters*, 104(16):164301, 2010. [DOI], [OA].
[44] L. Jaouen and F. Chevillotte. Length Correction of 2D Discontinuities or Perforations at Large Wavelengths and for Linear Acoustics. *Acta Acustica united with Acustica*, 104(2):243–250, 2018. [DOI].
[45] R. E. Collin. *Field theory of guided waves*. John Wiley & Sons, 1990.
[46] M.R. Stinson and E.A.G. Shaw. Acoustic impedance of small, circular orifices in thin plates. *Journal of the Acoustical Society of America*, 77(6):2039–2042, 1985. [DOI].